

Stiffening of under-constrained spring networks under isotropic strain

Cheng-Tai Lee and Matthias Merkel

*CNRS, Centre de Physique Théorique (CPT, UMR 7332), Turing Center for Living Systems,
Aix Marseille Univ, Université de Toulon, Marseille, France*

Disordered spring networks are a useful paradigm to examine the relation between microscopic material structure and macroscopic mechanical properties of amorphous materials. Here, we study the elastic behavior of under-constrained spring networks, i.e. networks with more degrees of freedom than springs. While such networks are usually floppy, they can be rigidified by applying external strain. Recently, an analytical formalism has been developed to predict the mechanical network properties close to this rigidity transition. We numerically show that these predictions apply to many different classes of spring networks, including phantomized triangular, Delaunay, Voronoi, and honeycomb networks. The analytical predictions further imply that the shear modulus G scales linearly with isotropic stress T close to the rigidity transition; however, this seems to be at odds with recent numerical studies suggesting an exponent between G and T that is smaller than one for some network classes. Using an increased numerical precision and shear stabilization, we demonstrate here that linear scaling, $G \sim T$, holds independent of the network class. Finally, we verify that our obtained scaling exponents remain valid in the limit of a large system size.

INTRODUCTION

Strain-induced macroscopic rigidity and its dependence on the microscopic structure in amorphous materials such as fibrous networks, glasses, jammed colloids, and granular materials have long been intriguing topics of research. While the macroscopic mechanics of crystalline materials can be computed explicitly by exploiting their spatially periodic microscopic structure, this is not possible for disordered materials. In particular, upon deformation disordered materials generally display non-affine microscopic displacements that are typically hard to predict [1–11].

A classical way to predict the onset of rigidity in many systems is to use Maxwell’s constraint counting, which states that rigidity emerges if the constraints in the system outnumber its degrees of freedom [12–14]. In systems with pair interactions, this is equivalent to comparing the average connectivity z , i.e. the average number of pair interactions each particle is involved in, to the number of degrees of freedom per particle, which is given by the dimension of space, D . Such systems are predicted to be rigid if z exceeds the isostatic point, $z > z_c := 2D$. In this case the system is called over-constrained. Otherwise, for $z < z_c$, the system is called under-constrained or sub-isostatic, and is predicted to be floppy. As a simple model to study the mechanics of amorphous materials, we discuss here strain-induced rigidity in under-constrained disordered spring networks [15–20].

While Maxwell’s constraint counting predicts under-constrained systems to be floppy, they can still be rigidified, either through the application of external strain or the presence of residual stresses [3, 6, 7, 11, 16, 19–23]. This is illustrated for both isotropic (i.e. bulk) and shear strain in Figure 1a. Beyond some critical strain value the applied strain induces internal stresses, which create finite bulk and shear moduli (Figure 1b).

Recent work involving one of us proposed a theoretical approach that allows to analytically predict the elastic

properties of athermal under-constrained materials close to the strain-induced rigidity transition [20]. This approach is based on a minimal-length function that formalizes the relationship between spring lengths and the applied strain. This minimal-length function both reflects the critical point where the network starts to rigidify and allows to predict the elastic network properties in the rigid regime. In Ref. [20], this approach was numerically verified both on models for disordered cellular materials and for packing-derived spring networks. However, it has never been explicitly tested for other classes of under-constrained spring networks.

Reference [20] predicts the behavior of the elastic moduli close to the transition, where the bulk modulus B shows as discontinuity, while the shear modulus G increases linearly with isotropic strain ε (Figure 1b). One can show that as a consequence of both, one would expect the shear modulus G to linearly increase also with isotropic stress T close to the transition. This is also consistent with earlier work on stress-induced rigidity [3, 21, 24]. However, more recent numerical work [19] on under-constrained disordered spring networks suggested that the value for the scaling exponent between G and T can differ from one, depending on the class of network studied. The reason for this deviation from the analytical predictions is so far unclear. Other recent work proposed that the numerical results in Ref. [20] could potentially be affected by finite-size effects caused by a diverging length scale when shearing the system [11]. Could similar finite-size effects be the reason for this contradiction between predicted and numerically obtained exponents between G and T ?

Here, we numerically test the predictions from Ref. [20] on several different classes of athermal spring networks. These include phantomized triangular, Delaunay, Voronoi, and honeycomb networks, where we study two types of spring potentials, harmonic and rope-like (Figure 1c). In the following, we first summarize the analytical approach from Ref. [20] in section I. We then

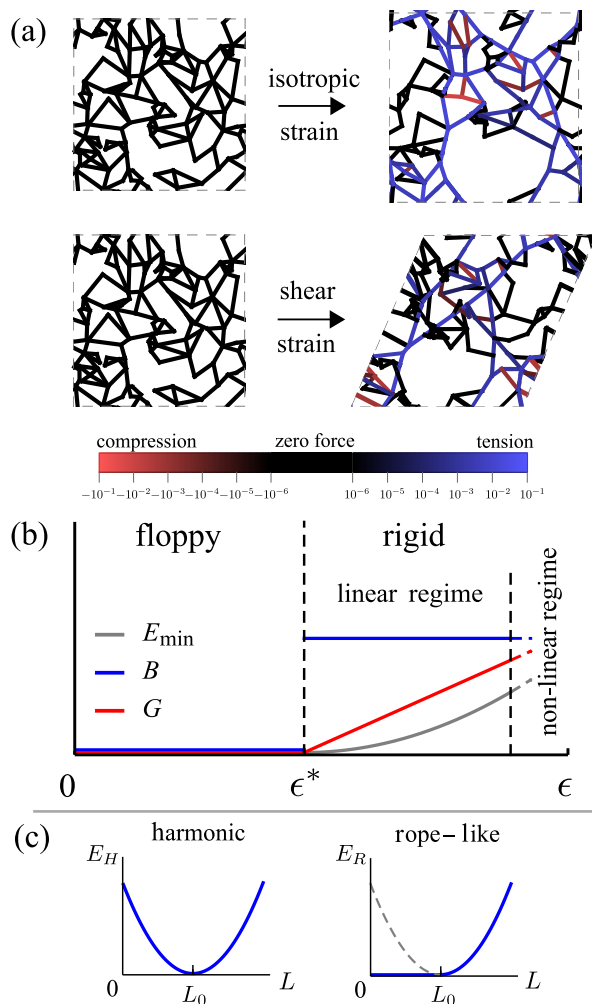


FIG. 1. Under-constrained spring networks can be rigidified by the external application of strain. (a) Network configurations and spring tensions for an example network under isotropic and shear strain. (b) Change of minimal network energy E , bulk modulus B , and shear modulus G when isotropically deforming a network across the rigidity transition, which occurs at the critical strain value ϵ^* . Below ϵ^* , all springs can attain their rest lengths, the system is floppy, and $E = B = G = 0$. Beyond ϵ^* , springs start to deviate from their rest lengths. According to Ref. [20], the bulk modulus B shows a discrete jump at ϵ^* , while G increases linearly and E increases quadratically with the distance from the transition point ϵ^* . (c) Two types of spring potentials are used in our simulations, harmonic (left) and rope-like (right), where L denotes spring length and L_0 spring rest length.

test the analytical predictions on several spring networks and show that they follow the predicted behavior (section II B). In section II C, we furthermore show that the scaling behavior of the coefficients appearing in the minimal-length function with connectivity z depends on the network class. We then numerically explore the scaling behavior of the shear modulus G over isotropic stress T with increased numerical precision and find a scaling exponent of one, independent of network class (sec-

tion II D). Moreover, we show that there is likely no diverging length scale for isotropic strain that would affect this result (section II E). Taken together, the analytical framework from Ref. [20] extends to all four network classes studied here.

I. THEORETICAL PREDICTIONS

We start by summarizing the approach of Ref. [20], which allows to predict the elastic properties of under-constrained spring networks close to the rigidity transition. In general, the formalism applies to any disordered Hookean spring network where each spring i has a different spring constant K_i and rest length L_{0i} . The energy of such a network is:

$$E = \sum_{i=1}^N K_i (L_i - L_{0i})^2, \quad (1)$$

where L_i denotes the length of spring i . The springs are connected at movable nodes, around which they can freely rotate. While the approach can be applied largely independently of the precise boundary conditions, we focus here on periodic boundary conditions with fixed system size.

Here, to explain just the key ideas of the approach, we focus for simplicity on the special case of a network with homogeneous spring constants $K_i = K$ and rest lengths $L_{0i} = L_0$:

$$E = K \sum_{i=1}^N (L_i - L_0)^2. \quad (2)$$

Note that also networks with heterogeneous spring properties can be formally mapped onto Eq. (2) as discussed in appendix A.

The elastic properties of disordered networks in mechanical equilibrium are in general difficult to predict analytically. Formally, these elastic properties can be computed from derivatives of a minimal energy function $E_{\min}(\epsilon, \gamma)$ with respect to external isotropic strain ϵ or shear strain γ . This function corresponds to the minimized system energy $E(\{\mathbf{r}_n\}, \epsilon, \gamma)$ with respect to the node positions \mathbf{r}_n at constant strain variables ϵ, γ . However, applying strain to a disordered network generally induces non-affine displacements of the node positions, which are typically hard to predict without explicit numerical energy minimization. To still make non-trivial predictions about the elastic network properties, Ref. [20] introduced a different approach. Instead of explicitly following the node motion, progress can already be made by focusing on the relation between spring lengths L_i and external strain.

Note that while we focus in this section on harmonic springs, the formalism can also be applied to networks with rope-like pair interactions (Figure 1c). This is because a rope-like pair interaction can be perfectly mim-

icked by a chain of two or more harmonic springs [20] (see also appendix D).

A. Key idea

To obtain an explicit expression for E_{\min} in terms of external strain, we first transform the expression in Eq. (2) into a sum of two squares:

$$E = NK \left[(\bar{L} - L_0)^2 + \sigma_L^2 \right]. \quad (3)$$

Here, $\bar{L} = (\sum_i L_i)/N$ and $\sigma_L^2 = (\sum_i [L_i - \bar{L}]^2)/N$ are average and variance of the spring lengths, respectively.

The expression in Eq. (3) allows us to more conveniently discuss the minimal network energy E_{\min} and its behavior once we strain the system. Because E is the sum of two squares, an energy minimum is attained whenever both $|\bar{L} - L_0|$ and σ_L are as small as possible. There are two possibilities. First, if there is a set of node positions such that both squares can simultaneously attain zero, then the minimal energy is zero $E_{\min} = 0$. Because elastic stresses and moduli correspond to derivatives of E_{\min} , the system is floppy in this parameter regime. Second, there might be *no* set of node positions such that both terms $|\bar{L} - L_0|$ and σ_L can simultaneously vanish. In this regime, the system is typically rigid.

To access the value of E_{\min} in the rigid regime, we need to understand how the system compromises between minimizing $|\bar{L} - L_0|$ and σ_L in Eq. (3). To this end, we first need a way to express which combinations of \bar{L} and σ_L are geometrically possible. As shown in Ref. [20], this can be done using a minimal-length function $\bar{L}_{\min}(\sigma_L)$ that depends on σ_L : A combination of \bar{L} and σ_L is *geometrically possible* only if:

$$\bar{L} \geq \bar{L}_{\min}(\sigma_L). \quad (4)$$

For instance, for $\sigma_L = 0$ it is possible to find network configurations with $\bar{L} \geq L_0^* := \bar{L}_{\min}(\sigma_L = 0)$. Thus, for $L_0 \geq L_0^*$ the network will be floppy, because both squares in Eq. (3) can simultaneously vanish, which implies that E_{\min} and its derivatives vanish. We say that, for such values of L_0 , all springs are *geometrically compatible* with each other. Conversely, for $L_0 < L_0^*$, both squares can not simultaneously vanish, and the springs are *geometrically incompatible* with each other. Note that the function $\bar{L}_{\min}(\sigma_L)$ and Eq. (4) reflect which combinations of (\bar{L}, σ_L) are *geometrically possible*, independently of L_0 . Meanwhile, the parameter L_0 controls whether the system is in a *geometrically compatible* or *incompatible* state.

In general, the precise functional form of $\bar{L}_{\min}(\sigma_L)$ depends on the network structure. However, we showed in Ref. [20] that to first order in σ_L it can be expanded as

$$\bar{L}_{\min}(\sigma_L) = L_0^* - a_\ell \sigma_L, \quad (5)$$

where L_0^* and a_ℓ are constants that encode the network structure. Eq. (5) holds in the limit of small σ_L , which

means that the system is close to the transition point, where $\sigma_L = 0$.

Finally, to derive an expression for the minimal energy E_{\min} in the geometrically incompatible regime, we combine two parts: the energy in Eq. (3) and the condition of geometrically possible combinations (\bar{L}, σ_L) in Eqs. (4) and (5). First, Eq. (4) implies that for fixed σ_L , the energy in Eq. (3) is minimized when $\bar{L} = \bar{L}_{\min}(\sigma_L)$. Combining this with Eq. (5), insertion into Eq. (3), and minimization with respect to σ_L , yields:

$$E_{\min} = \frac{NK}{1 + a_\ell^2} (L_0^* - L_0)^2. \quad (6)$$

This expression only depends on the spring number N , the spring constant K , the rest length L_0 , and the two parameters L_0^* and a_ℓ that encode the network structure. Note that from Eq. (6) we see that the system energy is that of an effective single spring with rest length L_0 .

B. Simple example network

To illustrate the ideas of the previous section, we discuss a simple example network (Figure 2a left). The network consists of four springs with equal spring constants K and rest lengths L_0 . Two of the springs are connected to fixed points (black dots) located at positions $(-L_x/2, 0)$ and $(L_x/2, 0)$, respectively. The two internal nodes (red dots) at positions \mathbf{r}_n with $n = 1, 2$ are movable. We will use the ideas of the previous section to derive an expression for the minimal energy E_{\min} .

For $L_0 \geq L_x/3$, there are always configurations where all springs can attain their rest lengths $L_i = L_0$ (Figure 2a top). This implies that $|\bar{L} - L_0| = 0$ and $\sigma_L = 0$, i.e. both terms in Eq. (3) can simultaneously vanish.

Conversely, for $L_0 < L_x/3$, the system is in the geometrically incompatible regime. Our 4-spring example network is simple enough so that we can explicitly minimize the energy with respect to the inner node positions $\mathbf{r}_n = (x_n, y_n)$ with $n = 1, 2$. This will allow us to first directly test whether the minimal energy has the form predicted by Eq. (6) in the previous section. The energy of our example network is

$$E = K \left[\left(x_1 + \frac{L_x}{2} - L_0 \right)^2 + 2 \left(x_2 - x_1 - L_0 \right)^2 + \left(\frac{L_x}{2} - x_2 - L_0 \right)^2 \right]. \quad (7)$$

Here, to simplify the following discussion, we have set $y_1 = y_2 = 0$. The energy E has a global minimum at $x_1 = -(L_x + 2L_0)/10$, $x_2 = (L_x + 2L_0)/10$, where its value is

$$E_{\min} = \frac{2K}{5} (L_x - 3L_0)^2. \quad (8)$$

This expression is indeed of the predicted form Eq. (6).

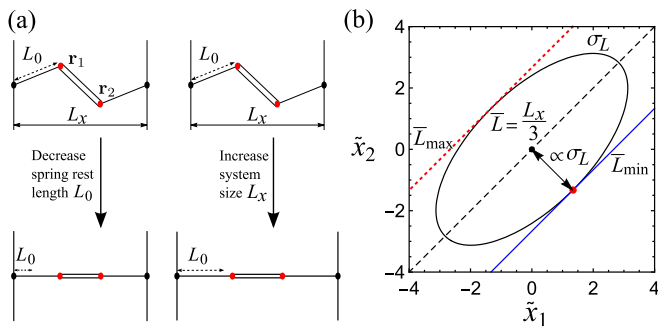


FIG. 2. Illustration of the analytical formalism using a 4-spring example network. (a) The network can be rigidified by either decreasing the spring rest length L_0 or, equivalently, increasing the wall distance L_x . Black and red dots indicate fixed and movable internal nodes, respectively. (b) Dependence of average \bar{L} and standard deviation σ_L of the four spring lengths on the internal node positions $\mathbf{r}_n = (x_n, y_n)$ with $i \in \{1, 2\}$ and $y_1 = y_2 = 0$. The axes are $\tilde{x}_1 = x_1 + L_x/6$ and $\tilde{x}_2 = x_2 - L_x/6$. Curves of constant \bar{L} are diagonal lines (e.g. with decreasing \bar{L} : red dotted, black dashed, blue solid lines), while curves of constant σ_L are ellipses whose linear size scales with σ_L . The minimal \bar{L} for given σ_L (black ellipse) corresponds thus to the red dot. As a consequence, the minimal \bar{L} for given σ_L decreases linearly with σ_L .

We now demonstrate how the minimal energy E_{\min} can instead be obtained using the ideas of the previous section. We first discuss which pairs of \bar{L} and σ_L are geometrically possible. To this end, we express \bar{L} and σ_L in terms of the internal degrees of freedom x_1, x_2 :

$$\bar{L} = \frac{L_x}{3} + \frac{1}{4}(\tilde{x}_2 - \tilde{x}_1), \quad (9)$$

$$\sigma_L^2 = \frac{1}{16}(11\tilde{x}_1^2 - 14\tilde{x}_1\tilde{x}_2 + 11\tilde{x}_2^2), \quad (10)$$

where we defined $\tilde{x}_1 = x_1 + L_x/6$ and $\tilde{x}_2 = x_2 - L_x/6$. Both Eqs. (9) and (10) are illustrated in Figure 2b. Curves of constant \bar{L} correspond to lines inclined by 45° , where \bar{L} increases as \tilde{x}_1 decreases and \tilde{x}_2 increases. Meanwhile, curves of constant σ_L correspond to ellipses centered at $\tilde{x}_1 = \tilde{x}_2 = 0$, whose main axes scale with σ_L and are oriented at 45° angles with respect to the \tilde{x}_1 and \tilde{x}_2 axes [25]. Thus, for a given value of σ_L , the combination of x_1 and x_2 can give rise to values for \bar{L} only in an interval between $\bar{L}_{\min}(\sigma_L)$ (blue solid line) and $\bar{L}_{\max}(\sigma_L)$ (red dashed line). The upper bound $\bar{L}_{\max}(\sigma_L)$ only exists because we set $y_1 = y_2 = 0$ before; without this constraint, \bar{L} can become arbitrarily large for a given σ_L [26]. Meanwhile, the lower bound $\bar{L}_{\min}(\sigma_L)$ decreases linearly with the distance between origin (black dot) and the intersection point (red dot) in Figure 2b, which is proportional to σ_L . This intersection point (red dot in Figure 2b) lies along the direction of the short axis length, i.e. on the ray $\tilde{x}_1 = -\tilde{x}_2$ with $\tilde{x}_1 > 0$. Insertion into Eqs. (9) and (10) yields:

$$\bar{L}_{\min}(\sigma_L) = \frac{L_x}{3} - \frac{\sigma_L}{3}. \quad (11)$$

This is of the form of Eq. (5), where we identify $L_0^* = L_x/3$ and $a_\ell = 1/3$. Inserting this into Eq. (6), we obtain indeed Eq. (8).

In our discussion here, we included the internal degrees of freedom x_1, x_2 to demonstrate their connection to geometrically possible combinations of \bar{L} and σ_L , and to obtain explicit values for L_0^* and a_ℓ . In general however, the approach from Ref. [20] does not require a discussion of internal degrees of freedom. Equations (3)–(5) are sufficient to understand the overall system behavior close to the rigidity transition, unless one wants to derive the values of the coefficients L_0^* and a_ℓ from first principles.

C. Effect of isotropic strain

We now discuss how to incorporate the effect of isotropic strain ϵ into the formalism. The 4-spring system in Figure 2a (left) transitions from floppy to rigid when decreasing the spring rest length L_0 , where the transition point $L_0^* = L_x/3$ scales with the system size L_x . As a consequence, the system can also be rigidified by instead increasing the system size L_x while keeping L_0 constant (Figure 2a right). This equivalence between using spring rest length L_0 or system size (i.e. bulk or isotropic strain) as the control parameter is best formalized by non-dimensionalizing the length units. Reference [20] defines the length unit $L_c := (V/N)^{1/D}$, where D is the dimension of space, V is the system volume, and N is the number of springs. With this length unit, the dimensionless spring rest length $\ell_0 \equiv L_0/L_c$ becomes a combined control parameter tuning the ratio between L_0 and linear system dimension.

We define (linear) isotropic strain as $\epsilon := (V/V_{\text{ref}})^{1/D} - 1$, where V_{ref} is the system volume at a reference state. Here, we use the system volume of the network right after creation as the reference volume V_{ref} . Hence, our combined control parameter depends on bulk strain ϵ as:

$$\ell_0 = \frac{L_0}{1 + \epsilon} \left(\frac{N}{V_{\text{ref}}} \right)^{1/D}. \quad (12)$$

In this paper, we discuss only two-dimensional networks, thus using $D = 2$, where V is the network area.

Using our length unit L_c , we introduce the re-scaled average $\bar{\ell} = \bar{L}/L_c$ and standard deviation $\sigma_\ell = \sigma_L/L_c$ of the spring lengths. Then Eq. (5) becomes:

$$\bar{\ell}_{\min}(\sigma_\ell) = \ell_0^* - a_\ell \sigma_\ell. \quad (13)$$

Here, $\ell_0^* = L_0^*/L_c$ corresponds to the transition point for the combined control parameter ℓ_0 . Therefore, ℓ_0^* does only depend on the network structure but not on system size. The isotropic strain where the network rigidifies is then, according to Eq. (12), $\epsilon^* = L_0/(\ell_0^* [V_{\text{ref}}/N]^{1/D}) - 1$.

Moreover, using L_c as length unit and KL_c^2 as energy unit, we obtain from Eq. (6) an explicit expression of the

system energy in terms of the combined control parameter ℓ_0 :

$$e_{\min}(\ell_0) = \frac{N}{(1+a_\ell^2)} (\ell_0^* - \ell_0)^2. \quad (14)$$

Thus, via Eq. (12), this equation provides an explicit expression of the dimensionless system energy on isotropic strain ϵ .

D. Effect of shear strain

To understand how shear strain enters the formalism, we first note that shearing the system does clearly not change the energy formula Eq. (3). However, shearing the system will change the set of geometrically possible combinations (ℓ, σ_ℓ) . Thus, shear strain needs to be included as a parameter in the minimal-length function $\bar{\ell}_{\min}$. In Ref. [20] this function is Taylor expanded to second order in shear strain, so that Eq. (13) becomes most generally:

$$\bar{\ell}_{\min}(\sigma_\ell, \hat{\gamma}) = \hat{\ell}_0^* - a_\ell \sigma_\ell + b_1 \hat{\gamma} + b \hat{\gamma}^2. \quad (15)$$

For later compactness of notation, here we also substituted the notation of parameter ℓ_0^* by $\hat{\ell}_0^*$.

Note that the linear order term in $\hat{\gamma}$ appears only because disordered systems with a finite size generally display a small but finite anisotropy. Eq. (15) can be simplified by removing this anisotropy through defining a new shear variable $\gamma = \hat{\gamma} - \Delta\gamma_0$, where $\hat{\gamma} = \Delta\gamma_0$ is defined as the shear where the function $\bar{\ell}_{\min}(\sigma_\ell, \hat{\gamma})$ is minimal: $\Delta\gamma_0 = -b_1/2b$. Defining $\ell_0^* := \hat{\ell}_0^* - b_1^2/4b$, this leads to the minimal-length function:

$$\bar{\ell}_{\min}(\sigma_\ell, \gamma) = \ell_0^* - a_\ell \sigma_\ell + b\gamma^2. \quad (16)$$

The anisotropy $\Delta\gamma_0$ is expected to disappear in the limit of a large network size.

E. Elastic properties near the rigidity transition

Combining Eq. (16) with the dimensionless form of Eq. (3) and minimizing with respect to σ_ℓ , we obtain the following explicit energy expression in terms of the control parameters ℓ_0 and γ :

$$e_{\min}(\ell_0, \gamma) = \frac{N}{1+a_\ell^2} (\ell_0^* - \ell_0 + b\gamma^2)^2. \quad (17)$$

Derivatives of this expression with respect to ℓ_0 (which is related to isotropic strain ϵ via Eq. (12)) and shear strain γ allow to derive the following quantities, here for the 2D

case [20]:

$$T/K = \frac{\ell_0^*}{1+a_\ell^2} (\ell_0^* - \ell_0 + b\gamma^2), \quad (18)$$

$$\sigma/K = \frac{4b\gamma}{1+a_\ell^2} (\ell_0^* - \ell_0 + b\gamma^2), \quad (19)$$

$$\Delta B/K = \frac{(\ell_0^*)^2}{2(1+a_\ell^2)} \text{ at } \gamma = 0, \quad (20)$$

$$G/K = \frac{4b}{1+a_\ell^2} (\ell_0^* - \ell_0 + 3b\gamma^2). \quad (21)$$

Here, T , σ , ΔB and G are (dimensional) isotropic stress, shear stress, bulk modulus discontinuity, and shear modulus, respectively. These formulas hold close to the rigidity transition in the region where Eq. (16) is accurate. As shown by Eqs. (18)–(21), the three parameters ℓ_0^* , a_ℓ , and b fully encode how the microscopic structure affects the macroscopic elastic behavior in this regime.

II. NUMERICAL RESULTS

While in Ref. [20] the analytical predictions in Eqs. (18)–(21) were numerically tested on packing-derived networks only, we test these predictions here on a set of additional network classes. These include phantomized triangular and Delaunay networks (both with varying connectivity z), as well as honeycomb and Voronoi networks (which both have fixed connectivity $z = 3$). Here we probe the elastic properties of these networks under isotropic (i.e. bulk) strain.

A. Network generation and energy minimization

Networks of freely hinging nodes are created in a periodic box following existing protocols [19, 27] (details in appendix B). We probe the system by varying isotropic strain ϵ . Each time, we first use bisection to detect the transition point ϵ^* , before we carry out exponential and/or linear sweeps in isotropic strain ϵ (details in appendix C). To ensure high precision in our energy minimization, we use an optimized conjugate gradient scheme that allows to reduce the average residual force per degree of freedom to less than 10^{-12} [20].

Right after creation, where $\hat{\gamma} = 0$, the disordered networks will generally display an anisotropy. To remove this anisotropy, we need to shear the system to the state $\hat{\gamma} = \Delta\gamma_0$ (i.e. $\gamma = 0$, see section ID). At this point, according to Eq. (19), shear stress vanishes, $\sigma = 0$. Thus, the anisotropy in the networks can be numerically removed using shear stabilization [28]. Shear stabilization means that shear strain is treated as an additional degree of freedom during the energy minimization. Unless stated otherwise, we always apply this method during the bisection phase to search for the transition point, so that our system right after the bisection phase is at

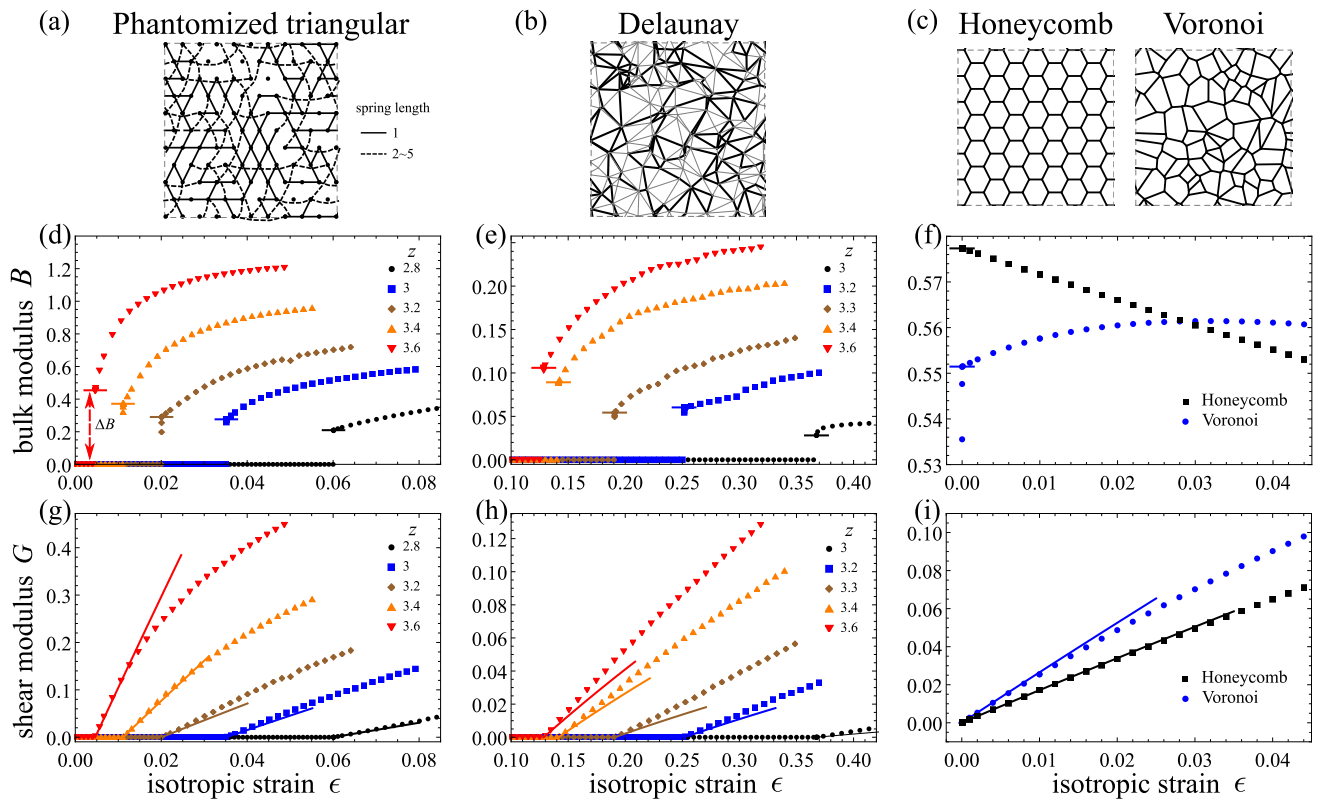


FIG. 3. Behavior of bulk and shear modulus across the transition for four different classes of networks and comparison to analytical predictions. (a)-(c) Sketches of network structures of phantomized triangular (a, $z = 3.2$, $W = 10$), Delaunay (b, $z = 3.2$, $W = 12$), Voronoi (c, $z = 3$, $W = 12$) and honeycomb (c, $z = 3$, $W = 12$) networks. In (a), the solid lines are springs of length one, while the dashed ones are phantomized springs, i.e. springs that cross one or more nodes without being connected to them. While phantomized springs are actually straight – they are shown slightly curved only for better visualization. In (b), gray lines indicate the removed springs from the initial full Delaunay network, leaving the black springs in the actual network. (d)-(i) Numerically obtained bulk modulus B and shear modulus G at $\gamma = 0$ against increasing isotropic strain ϵ for different network classes: phantomized triangular (d, g, $W = 40$) and Delaunay (e, h, $W = 20$) networks with variable connectivity z , as well as Voronoi (f, i, $W = 70$) and honeycomb (f, i, $W = 60$). Here, we use harmonic spring potentials, and we shear stabilized the networks before the ϵ sweeps (appendix C). The discontinuity ΔB in the bulk modulus at the transition point and linear scaling of G predicted from Eqs. (20) and (21) are indicated as solid bars and solid lines, respectively.

$(\epsilon, \gamma) = (\epsilon^*, 0)$. During the subsequent ϵ sweeps, we keep shear strain γ fixed (details in appendix C).

B. Elastic moduli close to the transition

To numerically characterize the nature of the transition, we first carry out a combination of exponential and linear sweeps around the transition point ϵ^* (details in appendix C). In Figure 3, we plot bulk modulus B and shear modulus G against isotropic strain ϵ for single network realizations with varying connectivity z , where we use harmonic spring potentials.

At the transition, all networks show a discontinuity ΔB in the bulk modulus. In contrast, the transition in the shear modulus G is continuous at ϵ^* . This is qualitatively consistent with our analytical predictions (section IE) and the behavior of packing-derived networks [20]. We also observe that for both phantomized tri-

angular and Delaunay networks the transition point ϵ^* increases with the average connectivity z .

To compare these data to a quantitative prediction for the bulk modulus discontinuity ΔB according to Eq. (20), we need the values of ℓ_0^* and a_ℓ for our simulations. We extract ℓ_0^* using the value ϵ^* of the isotropic strain at the transition point and insert it in Eq. (12). To extract a_ℓ , we plot σ_ℓ over $\bar{\ell} - \ell_0$ (inset of Figure 4d) and perform a linear fit whose slope is a_ℓ for small $\bar{\ell} - \ell_0$ (see appendix D). Note that for symmetry reasons, the honeycomb lattice has $\sigma_\ell = 0$ and thus $a_\ell = 0$. The resulting predictions for the bulk modulus discontinuities ΔB are respectively indicated as horizontal bars in Figure 3d-f. Indeed, our predictions match well the discontinuities present in the simulation data for all four network classes and all connectivities z . Note that some of the simulation data points right at the transition fall below the predicted value for ΔB , which is likely due to numerical residues [20].

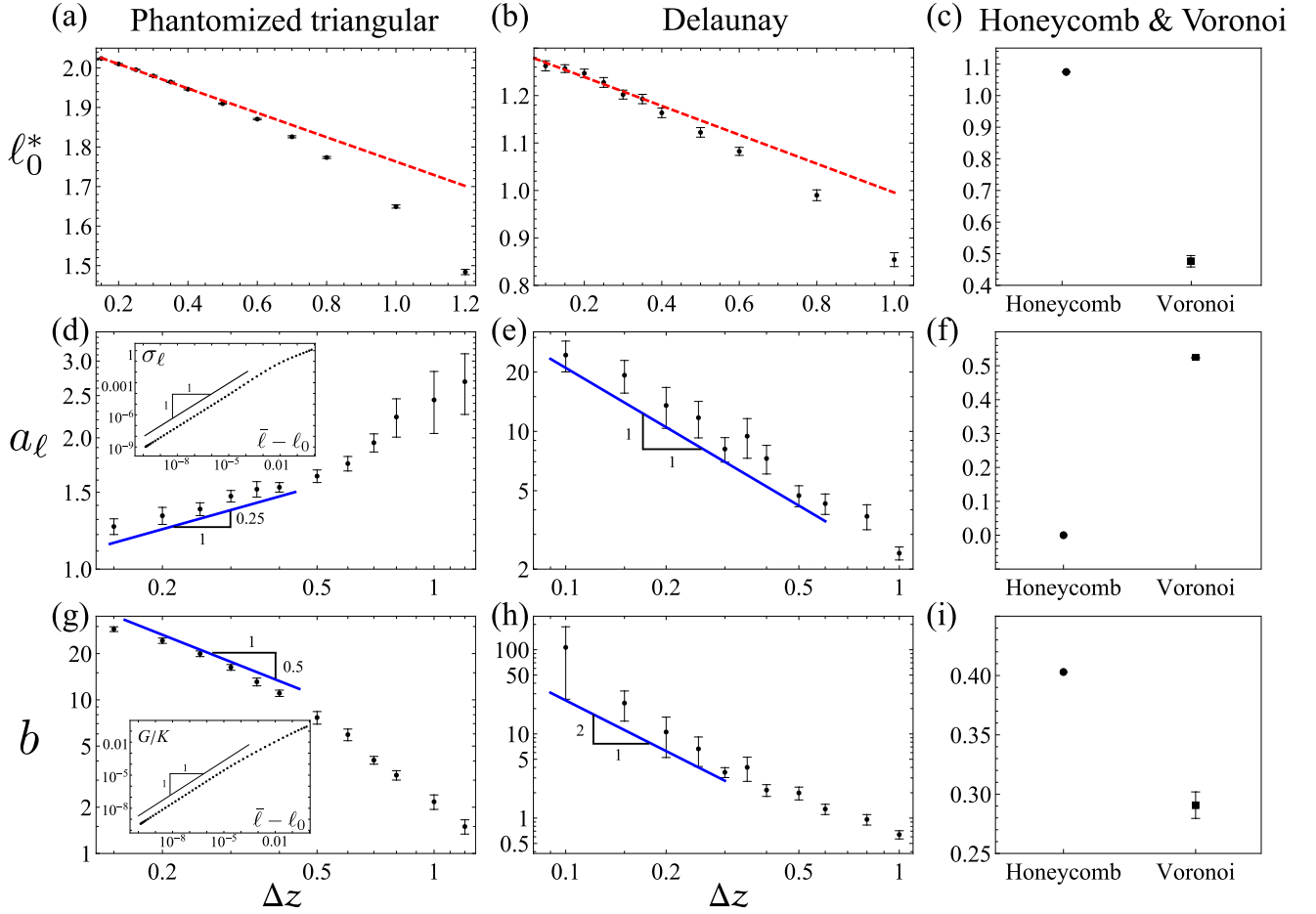


FIG. 4. Scaling of the parameters ℓ_0^* , a_ℓ and b with network connectivity z for phantomized triangular (system size $W = 40$), Delaunay ($W = 20$), Voronoi ($W = 70$; $z = 3$) and honeycomb ($W = 60$; $z = 3$) networks with harmonic spring potentials. The parameters ℓ_0^* , a_ℓ and b are extracted for each network realization according to the protocols in [section II B](#) and [appendix D](#). For instance (d inset) a_ℓ is extracted using a linear fit of σ_ℓ over $\bar{\ell} - \ell_0$, and (g inset) b is extracted using a linear fit of G over $\bar{\ell} - \ell_0$. Error bars in all panels indicate the standard error of the mean. We use the first 5 data points away from $\Delta z = 0$ to fit ℓ_0^* and obtain $2.07 - 0.31\Delta z$ for phantomized triangular and $1.30 - 0.30\Delta z$ for Delaunay networks (red dashed lines in panels (a) and (b)). For the honeycomb network, the numerically obtained value for ℓ_0^* is consistent with its theoretical value $\ell_0^* = 2^{1/2}/3^{1/4} \approx 1.0745$, and the parameter a_ℓ is exactly zero, because $\sigma_\ell = 0$ due to symmetry.

For the shear modulus, Eq. (21) predicts a continuous transition with a linear scaling $G \sim (\ell_0^* - \ell_0)$. Using Eq. (12), this implies also a linear scaling $G \sim \Delta\epsilon := \epsilon - \epsilon^*$ to lowest order in $\Delta\epsilon$. Indeed, this is what we observed close to the transition (inset of [Figure 4g](#)). We indicate this linear scaling also in [Figure 3g-i](#). Note that for larger $\Delta\epsilon$, non-linearities create deviations from this prediction.

Note that both honeycomb and Voronoi networks have their transition points at $\epsilon^* = 0$. This means that these networks at creation are able to support a finite global tension. In other words, it is possible to put a subset of the springs under tension while maintaining force balance on all internal nodes (i.e. there is a state of self stress [\[14\]](#)). While this is clearly the case for the honeycomb lattice, we show in [appendix E](#) that it is also true for any Voronoi network at creation.

Taken together, the elastic properties of the system close to the transition, such as the transition point ϵ^* , the magnitude of the discontinuity ΔB in the bulk modulus, and the linear scaling coefficient for the shear modulus G , can be predicted from the coefficients ℓ_0^* , a_ℓ , and b .

C. Scaling of ℓ_0^* , a_ℓ and b with connectivity z

In [Figure 4](#), we plot the parameters ℓ_0^* , a_ℓ and b for phantomized triangular, Delaunay, Voronoi, and honeycomb networks with harmonic spring potentials. For phantomized triangular and Delaunay networks, we show the dependency on the connectivity z . For the disordered networks (i.e. phantomized, Delaunay, and Voronoi) we average each time over 50 random realizations.

In both phantomized triangular and Delaunay net-

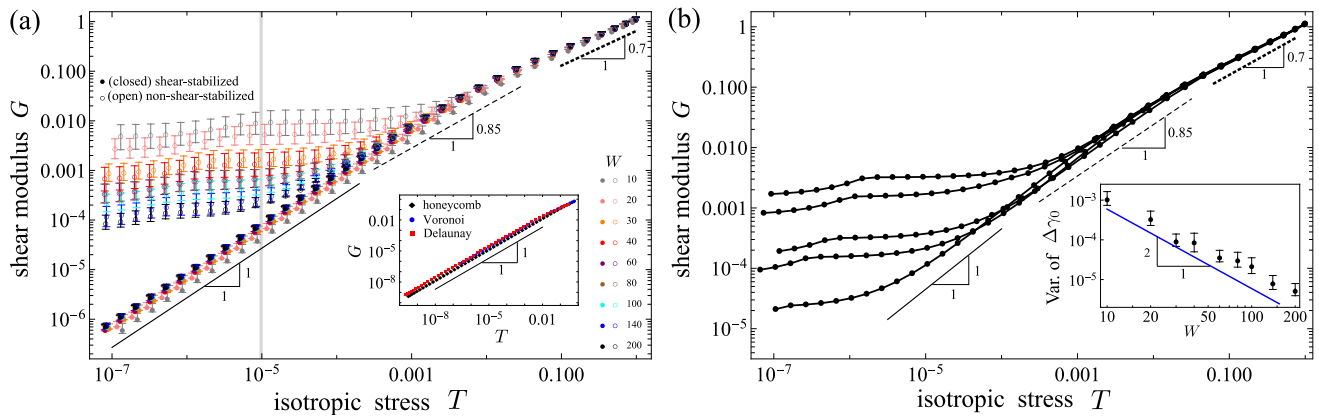


FIG. 5. The shear modulus G scales linearly with isotropic stress T for shear-stabilized networks. Without shear stabilization an additional plateau appears at small T . (a) Dependence of G on isotropic stress T for phantomized triangular networks with $z = 3.2$ and rope-like spring potentials for varying system size W , where we either use shear stabilization (closed circles) or not (open circles). All shear-stabilized networks show a linear scaling close to the transition point (at small T). The gray vertical line indicates the lowest T value probed in previous work [19]. (a inset) The linear scaling in $G(T)$ also appears for shear-stabilized honeycomb ($W = 60$), Voronoi ($W = 70$) and Delaunay ($W = 20$) networks. Error bars in panel a & inset indicate the standard error of the mean. (b) The $G(T)$ curves for individual phantomized triangular networks with $z = 3.2$ and $W = 40$ without shear stabilization also exhibit a plateau, confirming that the plateaus in panel a are not due to an averaging effect. (b inset) The variance of the network anisotropy $\Delta\gamma_0$ (defined below Eq. (15)) across different randomly generated networks for a given system size W scales inversely proportional with W^2 .

works, close to the isostatic point the parameter ℓ_0^* exhibits a linear dependence on Δz with a negative coefficient (Figure 4a,b), which has also been observed in 2D packing-derived networks [20].

In contrast, the z -scaling exponents of a_ℓ and b close to isostaticity depend strongly on the network class (Figure 4d,e,g,h). For instance for a_ℓ , we find for phantomized triangular networks a scaling exponent of ≈ 0.2 , for Delaunay networks, we find an exponent close to -1 , while we found an exponent of -0.5 in earlier work for packing-derived networks. Meanwhile for b , we find for phantomized triangular networks an exponent of ≈ -0.5 or smaller, for Delaunay networks an exponent of roughly -2 , while we have found before for packing-derived networks an exponent of -1 . Hence, these two parameters are sensitive to the microscopic network structure.

Note that for a small fraction of the Delaunay networks, we did not observe a linear scaling between σ_ℓ and $\bar{\ell} - \ell_0$, suggesting that the linear relation between $\bar{\ell}_{\min}$ and σ_ℓ might be violated for these networks (appendix D). A more detailed examination suggests that this could quite possibly be due to finite numerical cutoffs required to identify the transition point, which would make us miss the regime where this scaling is linear (appendix F). We excluded these networks from the averages shown in Figure 4. We stress that we only found deviations from the linear $\bar{\ell}_{\min}$ scaling for Delaunay networks with harmonic springs, while we could numerically confirm the predicted linear scaling for all phantomized triangular and Voronoi networks, as well as the honeycomb network.

D. The shear modulus scales linearly with isotropic stress.

In the previous sections (IE and IIB), we showed that the shear modulus G scales linearly with the isotropic strain beyond the transition point $\Delta\epsilon = \epsilon - \epsilon^*$. Moreover, a finite bulk modulus discontinuity at ϵ^* implies that also the isotropic stress T scales linearly with $\Delta\epsilon$ to lowest order, which can also be derived from Eqs. (12) and (18). Hence, we would expect from the analytical predictions in section I that the shear modulus scales linearly with the isotropic stress:

$$G \sim T^\alpha \quad \text{with } \alpha = 1. \quad (22)$$

However, recent numerical work has suggested different values for α . For instance, reference [19] studied networks with rope-like potentials, and for $z = 3.2$ the results suggested an exponent of $\alpha \approx 0.85$ for phantomized triangular and $\alpha \approx 0.9$ for Delaunay networks, while $\alpha = 1$ was found for honeycomb and Voronoi networks.

To resolve this contradiction between the numerical results from Ref. [19] and our analytical results from section I and Ref. [20], we simulate here different kinds of rope-like networks with a high numerical precision, where we vary linear system size W by more than an order of magnitude. Figure 5a shows the scaling of the shear modulus G against the isotropic stress T , both averaged over 50 realizations, for phantomized triangular networks, where we used two protocols. The open symbols correspond to a protocol without any shear stabilization. This means that no shear strain was applied after the creation of the network, and the ϵ sweep was

carried out at $\hat{\gamma} = 0$. The closed symbols correspond to a protocol where we used shear stabilization to find the transition point, and as a consequence the ϵ sweep was carried out at $\gamma = 0$ (see [section ID](#)).

We find that indeed, for the protocol with shear stabilization (closed symbols), the shear modulus G scales linearly with isotropic stress T over many orders of magnitude ([Figure 5a](#) & inset for the other network classes). This observation is independent of system size. However, without shear stabilization (open symbols), at small stress T we observe a plateau, whose value depends on system size. Away from the plateau regions the curves largely collapse for different system sizes.

The appearance of a plateau in $G(T)$ in the protocol without shear stabilization can be readily understood from our analytical results. [Eq. \(21\)](#) states that G is proportional to $\ell_0^* - \ell_0 + b\gamma^2$, where $(\ell_0^* - \ell_0) \sim \Delta\epsilon \sim T$ and $\gamma = \hat{\gamma} - \Delta\gamma_0$. Without shear stabilization, $\hat{\gamma} = 0$ and so $\gamma = -\Delta\gamma_0$. This implies a plateau in G that is proportional to $\Delta\gamma_0^2$. In other words, the plateau in $G(T)$ is related to the small anisotropy in the disordered networks. Shear stabilization removes this anisotropy and thus also the plateau in $G(T)$.

To test whether the plateaus that we find in [Figure 5a](#) do not result from an averaging effect, we plot in [Figure 5b](#) the same curves for individual realizations for a given system size. We find that the plateau is also present in individual simulations, and that its height fluctuates across realizations. This makes sense, because also the network anisotropy $\Delta\gamma_0$ fluctuates across realizations. Moreover, we find that the variance of $\Delta\gamma_0$ decreases inversely proportional to the number of springs in the system ([Figure 5b](#)), which scales as $\sim W^2$. Hence, the plateau in $G(T)$ corresponds to a finite-size effect. A similar conclusion was drawn also in [Ref. \[29\]](#) following a different line of argument.

E. The scaling exponents we observe are not due to finite-size effects.

In recent work, it was pointed out that scaling exponents in spring networks under shear strain may be affected by finite-size effects [[11](#)]. In particular, it was suggested that for networks of size W , finite-size effects could affect scaling exponents when shearing the systems by $\Delta\gamma \lesssim W^{-1/\nu}$ beyond the transition point γ^* , where $\nu > 0$. This would correspond to a diverging length scale $\xi \sim |\Delta\gamma|^{-\nu}$. While in this article, we probe the system mechanics with respect to isotropic strain ϵ instead, we still wanted to check whether such finite-size effects could affect our results.

Because the proposed finite-size scaling effects are due to a diverging length scale, they would likely affect not only the scaling of the shear modulus, but also other aspects of the system. For instance, the system mechanics with respect to isotropic strain is crucially determined by the minimal-length function $\bar{\ell}_{\min}$ depending on σ_ℓ in

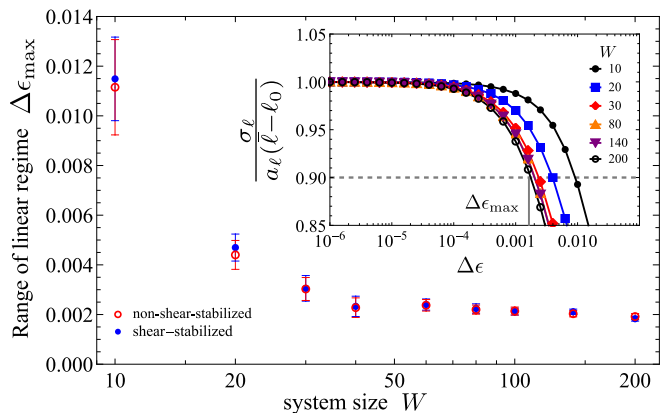


FIG. 6. The range of isotropic strain beyond the transition point, $\Delta\epsilon_{\max} = \epsilon_{\max} - \epsilon^*$, within which the linear scaling of the $\bar{\ell}_{\min}$ function holds for increasing system size, shown here for phantomized triangular networks with $z = 3.2$ and rope-like spring potentials. The range of linear scaling of the $\bar{\ell}_{\min}$ function is probed using the quotient $\sigma_\ell / (\bar{\ell} - \ell_0)$ ([appendix D](#)). In both cases $\Delta\epsilon_{\max}$ appears to approach an asymptotic value of $\approx 2 \times 10^{-3}$ as W increases, which indicates that the linear scaling of the $\bar{\ell}_{\min}$ function is not affected by a diverging length scale. Error bars indicate the standard error of the mean. (inset) $\Delta\epsilon_{\max}$ is defined as the strain range where the ratio $\sigma_\ell / (\bar{\ell} - \ell_0)$ shows a deviation of less than 10% from its value a_ℓ defined very close to the transition point ([appendix C](#)).

[Eq. \(13\)](#) ([section I](#)). Hence, we were wondering whether the linear scaling of $\bar{\ell}_{\min}$ with σ_ℓ is only valid close to the transition point with strains $\Delta\epsilon < \Delta\epsilon_{\max} \sim W^{-1/\nu'}$ for some $\nu' > 0$. In other words, we wondered whether the range $\Delta\epsilon_{\max}$ of linear $\bar{\ell}_{\min}$ scaling would algebraically decrease to zero with increasing system size W . In [appendix D](#), we show that the factor of proportionality a_ℓ in the $\bar{\ell}_{\min}$ function can be computed most precisely as $a_\ell = \sigma_\ell / (\bar{\ell} - \ell_0)$ at small $\Delta\epsilon$. We thus compute $\Delta\epsilon_{\max}$ as the strain where the quotient $\sigma_\ell / (\bar{\ell} - \ell_0)$ starts to differ by more than 10% from its value a_ℓ at small $\Delta\epsilon$ ([Figure 6](#) inset, details in [appendix C](#)).

In [Figure 6](#) we show the resulting dependency of $\Delta\epsilon_{\max}$ on system size W for phantomized triangular networks with rope-like spring potentials. While we observe an initial decrease in $\Delta\epsilon_{\max}$, our data is consistent with an approach to a finite asymptotic value of $\Delta\epsilon_{\max} \approx 2 \times 10^{-3}$ for large system size, both for shear-stabilized and non-shear-stabilized networks. This indicates that the linear scaling between $\bar{\ell}_{\min}$ and σ_ℓ , and thus likely also in $G(T)$, is not subject to the kind of finite-size effects that were discussed in [Ref. \[11\]](#) with respect to shear strain.

III. DISCUSSION

We studied the elastic behavior of sub-isostatic spring networks that are rigidified by isotropic expansion, comparing numerical simulation results with analytical pre-

dictions from Ref. [20]. We first summarized the approach from Ref. [20], which proposed an analytical framework to predict the mechanical properties of networks close to this rigidity transition based on a minimal-length function $\bar{\ell}_{\min}$ (Eq. (16)). We numerically verified the predicted linear scaling of the minimal-length function near the transition and extracted the three parameters ℓ_0^* , a_ℓ and b which together define the $\bar{\ell}_{\min}$ function and further allow to fully predict the elastic network properties close to the transition. For instance, Ref. [20] provides an expression for the discontinuity ΔB in the bulk modulus right at the transition point, which predicts well our numerical results (Figure 3). Moreover, we also recovered the predicted linear scaling of the shear modulus G with isotropic strain T close to the transition.

Next we explored the scaling of the parameters ℓ_0^* , a_ℓ and b with respect to connectivity z . We found that the scaling of the parameters a_ℓ and b with the distance to isostaticity $\Delta z = 4 - z$ strongly depends on the network class. We find that the scaling exponent for a_ℓ can even change sign, varying from -1 for Delaunay networks to ≈ 0.2 for phantomized triangular networks (Figure 4, with an exponent of -0.5 for packing-derived networks [20]). The scaling exponent for b varies from -2 for Delaunay networks to -0.5 for phantomized triangular networks (Figure 4, with an exponent of -1 for packing-derived networks [20]). This dependency on network class is not too surprising, since the parameters ℓ_0^* , a_ℓ and b depend on the microscopic network structure, which varies with network class. In contrast, the value of ℓ_0^* always showed a linear dependency on Δz , where intercept and slope depend on network class.

One prediction of the formalism in Ref. [20] is a linear scaling of the shear modulus G with the isotropic stress T close to the transition point: $G \sim T^\alpha$ with $\alpha = 1$. This is a direct consequence of the linear scaling of the shear modulus G with strain $\Delta\epsilon$ and the discontinuity ΔB in the bulk modulus. However, this prediction seems to be at odds with recent numerical work, which suggested that the value of α can be different from one for networks with a rope-like interaction potential, depending on the disordered nature of the network [19]. In particular, Ref. [19] found an exponent of $\alpha \approx 0.85$ for phantomized triangular networks and $\alpha \approx 0.9$ for Delaunay networks with connectivity of $z = 3.2$.

To reconcile the two results from Refs. [19, 20], we numerically studied the $G(T)$ scaling with an increased numerical precision, and our results confirmed the analytically-predicted scaling exponent of $\alpha = 1$ in both phantomized triangular and Delaunay networks (Figure 5a and inset). We show that the result also depends on a small random anisotropy in the generated network. In the presence of such a finite anisotropy, we observed a plateau in the shear modulus $G(T)$ for small isotropic stress T , consistent with the analytic prediction, Eq. (21). This plateau disappears when using shear stabilization [28], which removes the network anisotropy

by shearing the network by a shear strain $\Delta\gamma_0$ (section ID). We moreover show that the plateau disappears for larger system sizes (Figure 5b inset). Hence, while without shear stabilization large system sizes are required to probe the behavior close to the transition, shear stabilization allows to explore this regime already for smaller systems.

We see two possible reasons for the discrepancy in the $G(T)$ scaling between Refs. [19, 20]. First, we used the conjugate gradient minimizer code developed in Ref. [20], which allows us to probe the system at least two orders of magnitude closer to the transition point than Ref. [19] (see gray vertical line in Figure 5a). For instance in phantomized triangular networks we observe an exponent of $\alpha < 1$ for larger isotropic stress $T \gtrsim 10^{-3}$, which seems consistent with the value of 0.85 given by Ref. [19], while we observe an exponent of $\alpha = 1$ for stress T smaller than that. Second, we show that a small anisotropy in the generated network can lead to a plateau in the shear modulus curve $G(T)$, which could in turn affect the inferred scaling exponent.

Previous work suggested that finite-size effects could affect scaling exponents in spring networks [11]. This can occur whenever the system size is on the order of or smaller than a length scale that diverges close to the transition point. While Ref. [11] focused on shear simulations, we wanted to test whether such an effect could arise in our isotropic strain simulations. To this end, we numerically tested in what range around the transition point the linear scaling of the $\bar{\ell}_{\min}$ function holds, and our results suggest that this range does not decrease below a minimal strain difference of $\Delta\epsilon \approx 2 \times 10^{-3}$ for increasing system size (Figure 6). This indicates that the linear $\bar{\ell}_{\min}$ scaling is still valid for large system sizes. This is also consistent with Figure 5a, which shows that the $G(T)$ scaling is largely independent of system size.

ACKNOWLEDGEMENTS

We thank Martin Lenz for fruitful discussions. We thank the Centre Interdisciplinaire de Nanoscience de Marseille (CINaM) for providing us with office space. The project leading to this publication has received funding from the ‘‘Investissements d’Avenir’’ French Government program managed by the French National Research Agency (ANR-16-CONV-0001) and from ‘‘Excellence Initiative of Aix-Marseille University - A*MIDEX’’. The Centre de Calcul Intensif d’Aix-Marseille is acknowledged for granting access to its high-performance computing resources.

Appendix A: Generalization to networks with heterogeneous spring constants and rest lengths

In the main text, we focused on the case where all springs share the same rest length L_0 and the same spring

constant K . Here, we generalize this to networks where rest length and spring constant may differ among the springs. The energy for such heterogeneous networks, Eq. (1), can also be expressed in the same form as Eq. (3), where only the average and standard deviation of spring lengths need to be defined slightly differently.

Similar to Ref. [20], to generalize the approach with homogeneous rest lengths and spring constants, we aim to introduce re-scaled spring lengths \tilde{L}_i , re-scaled spring constants \tilde{K}_i , and an average spring length L_0 in a way that allows us to write the system energy, Eq. (1), in the form:

$$E = \sum_{i=1}^N \tilde{K}_i (\tilde{L}_i - L_0)^2. \quad (\text{A1})$$

For this to work, we need to define the re-scaled spring lengths as

$$\tilde{L}_i = L_i \frac{L_0}{L_{0i}}. \quad (\text{A2})$$

This will accordingly give rise to a new re-scaled spring constant

$$\tilde{K}_i = K_i \left(\frac{L_{0i}}{L_0} \right)^2. \quad (\text{A3})$$

Finally, we choose to define L_0 as the quadratic mean of the L_{0i} , weighted by the K_i :

$$L_0 = \sqrt{\frac{\sum_i K_i L_{0i}^2}{\sum_i K_i}}. \quad (\text{A4})$$

Using the re-scaling Eqs. (A2)–(A4), Eq. (1) can be exactly re-expressed as Eq. (A1). This network energy can be transformed into

$$E = NK \left[(\bar{L} - L_0)^2 + \sigma_L^2 \right]. \quad (\text{A5})$$

Here, we introduced the average spring constant $K := \sum_i K_i / N$, while \bar{L} and σ_L are defined as the average and standard deviation of the re-scaled spring length \tilde{L}_i with the weighting factors $W_i = \tilde{K}_i$:

$$\bar{L} := \frac{\sum_i W_i \tilde{L}_i}{\sum_i W_i}; \quad \sigma_L^2 := \frac{\sum_i W_i (\bar{L} - \tilde{L}_i)^2}{\sum_i W_i}. \quad (\text{A6})$$

We further use the the same length scale L_c given above Eq. (13), and the average spring constant K for non-dimensionalization of the system. Subsequently, the discussion in sections IC–IE remain unchanged.

Appendix B: Network generation

Networks are created according to the following protocols.

Phantomized triangular (Figure 3a) [27]: Following Ref. [19], a 2D triangular lattice of spacing 1 is first constructed by depositing three sets of W parallel filaments each at angles of 0° , 60° and 120° with the x -axis, respectively. To reduce the connectivity from $z = 6$ to values observed in e.g. collagen networks [30] of $3 \leq z < 4$, we first detach at each node one filament to create a network of homogeneous connectivity $z = 4$. To avoid system-spanning filaments, one spring is removed at a random position on each filament, giving the average connectivity $z = 4 - 6/W$. To further reduce the connectivity to a defined value z , we implement an iterative procedure. At each iteration, we randomly remove only a few of the springs and then clear off all of the dangling springs and isolated islands. This is repeated until the desired connectivity z is reached.

Delaunay (Figure 3b): Delaunay networks are constructed from W^2 nodes that were placed at uncorrelated random positions in a square box of side W . The connectivity of initially $z = 6$ is decreased to the desired value z by employing the same protocol using random cuts as for the phantomized networks.

Honeycomb (Figure 3c): We construct a network of $W^2/3$ regular hexagons with side length 1.

Voronoi (Figure 3c): Voronoi networks correspond to the Voronoi tessellation of $W^2/2$ nodes at uncorrelated random positions in a square box of side W . In all four network classes, we set the spring rest lengths L_{0i} to the respective initial spring lengths before any deformation is applied, and the spring constants to $K_i = 1/L_{0i}$.

Appendix C: Details of numerical strain sweeps and computation of the elastic moduli

In this paper, we exclusively carry out sweeps of isotropic strain ϵ , where before each sweep, we first identified the transition point ϵ^* . To this end, we implemented a bisection scheme, which we optimized by linearly interpolating the transition point in each step. We defined networks as rigid whenever their isotropic stress T is above a cutoff value of 10^{-10} (two orders of magnitude above the tolerance for the residual force cutoff per degree of freedom, 10^{-12}). We use isotropic stress T as a criterion for network rigidity, because it is much faster to compute than an elastic modulus.

In the bisection to identify the transition point, we also implemented the option to perform shear stabilization (sections ID and IIA) to remove network anisotropy. This is done by treating the shear strain $\hat{\gamma}$ as an additional degree of freedom during each energy minimization of the bisection process. In any case, shear stabilization was always turned off (i.e. shear remains constant) after the transition point ϵ^* has been identified.

We apply an exponential sweep of isotropic strain to probe the scaling behavior of network mechanics close to the transition point ϵ^* . In particular, we probed strain values $\epsilon - \epsilon^* = 10^{-10+0.2n}$, where the step index

n ranged from 0 to 51 by default, with only two exceptions. First, in [Figure 3](#), we apply the same exponential sweep, yet with n ranging from 0 to 7 only, which is then followed by a linear sweep. Second, for the Voronoi networks of size $W = 70$ ([Figure 4](#) and [Figure 5a](#) inset) we needed to increase the residual force cutoff for the energy minimization to 10^{-10} , and so we also raised the cutoff in isotropic stress T to identify the transition point to 10^{-8} . Accordingly, we changed the sweep to the values $\epsilon - \epsilon^* = 10^{-8+0.2n}$ with n ranging from 0 to 41.

We computed the elastic moduli using two different methods. For not too big networks, we diagonalized the Hessian of the system energy and used the resultant eigenvalues to compute elastic moduli [[20](#), [24](#), [31–33](#)]. This approach produces a higher numerical precision and was suitable for typical system sizes $W < 100$ ([Figure 3](#) and [4](#)). However, in [Figure 5](#) we studied networks with a large system size, and so we used a less time-intensive way of computing the shear modulus G . We computed G through a difference quotient of the shear stress over the shear strain: $G(\epsilon, \gamma = 0) = [\sigma(\epsilon, \Delta) - \sigma(\epsilon, -\Delta)]/2\Delta$, where we numerically tuned and found the optimized shear strain $\Delta = 5 \times 10^{-5}$. We also noticed that for $\epsilon - \epsilon^* < 10^{-7}$ the shear modulus computed with this method could deviate significantly from the true value. We hence excluded these data points in [Figure 5](#) and the lowest isotropic stress there is accordingly $T \approx 10^{-7}$.

Appendix D: Extraction of the parameters a_ℓ and b of the minimal-length function

To extract a_ℓ from numerical data, one could just directly use the $\bar{\ell}_{\min}(\sigma_\ell)$ function (Eq. [\(13\)](#)). However, this approach depends on the correct identification of the transition point ℓ_0^* . While we can identify ℓ_0^* with a relatively high precision of $\sim 10^{-10}$, we could even remove the dependency on ℓ_0^* entirely when determining a_ℓ . To this end, we note that in an energy-minimized state, the energy is also minimal with respect to variation of σ_ℓ , i.e. $dE/d\sigma_\ell = 0$. From Eq. [\(3\)](#), and using the insight that $\bar{\ell} = \bar{\ell}_{\min}(\sigma_\ell)$ in the rigid regime, the minimization condition reads:

$$\frac{dE}{d\sigma_\ell} = 2NK L_c^2 \left[(\bar{\ell} - \ell_0) \frac{d\bar{\ell}_{\min}}{d\sigma_\ell} + \sigma_\ell \right] = 0. \quad (\text{D1})$$

Using Eq. [\(13\)](#), the derivative of the minimal-length function is $d\bar{\ell}_{\min}/d\sigma_\ell = -a_\ell$. Taken together, we thus obtain the linear relation:

$$\sigma_\ell = a_\ell (\bar{\ell} - \ell_0). \quad (\text{D2})$$

Based on Eq. [\(D2\)](#), examining the relation between σ_ℓ and $(\bar{\ell} - \ell_0)$ (e.g. [Figure 4d](#) inset) allows both to effectively verify the scaling of the minimal-length function (Eq. [\(13\)](#)), and to extract the value of a_ℓ . This approach does not involve the critical value ℓ_0^* which we obtain with a lower precision as compared to $\bar{\ell}$ and σ_ℓ (as precise as 10^{-12}).

To extract the parameter b , we use the derived shear modulus formula (Eq. [\(21\)](#)), instead of directly using the original minimal-length function (Eq. [\(16\)](#)) since we do not shear the networks (i.e. $\gamma = 0$). As before, we intend not to use the critical value ℓ_0^* . Thus, to replace the term $(\ell_0^* - \ell_0)$ that appears in the shear modulus formula (Eq. [\(21\)](#)), we insert Eq. [\(D2\)](#) back into the minimal-length function (Eq. [\(13\)](#)) and obtain

$$\ell_0^* - \ell_0 = (1 + a_\ell^2) (\bar{\ell} - \ell_0). \quad (\text{D3})$$

Combining this equation with the shear modulus formula (Eq. [\(21\)](#)) yields

$$G/K = 4b (\bar{\ell} - \ell_0). \quad (\text{D4})$$

We used this equation to extract b from the plots of G over $\bar{\ell} - \ell_0$ ([Figure 4g](#) inset).

By default we use the first 25 data points from an exponential sweep to numerically fit Eqs. [\(D2\)](#) and [\(D4\)](#) and extract the parameters a_ℓ and b . Note that a_ℓ in [Figure 6](#) is defined in the very same way, based on the first 25 data points of an exponential sweep. Meanwhile in [Figure 3](#) we use only the first 5 data points due to a decreased step number n in the exponential sweep of isotropic strain (appendix [C](#)).

We note that rope-like spring potentials can be treated as well with the analytical framework in [section I](#), which we took into account when computing $\bar{\ell}$ and σ_ℓ here. While one way to treat rope-like spring potentials was discussed in Ref. [[20](#)], where each spring is subdivided into a series of shorter springs, we chose here an alternative approach. We used the fact that for rope-like spring potentials, a spring i only affects the mechanics when $L_i > L_{0i}$, while springs with $L_i < L_{0i}$ do not contribute. Thus, to compute $\bar{\ell}$ and σ_ℓ , whenever for any spring i the distance of the two connected nodes is smaller than the rest length L_{0i} , we set the spring length to $L_i = L_{0i}$. This redefinition of L_i does not affect the computation of shear modulus G and tension T .

Appendix E: Any Voronoi network has a state of self stress at creation.

We numerically found that Voronoi networks have a critical isotropic strain very close to zero, $\epsilon^* \approx 0$. Here we show that the critical strain is indeed exactly zero, by proving that there is a state of self stress right at creation of these networks [[14](#)]. In other words, at creation ($\epsilon = 0$) these networks can sustain finite tensions in a subset of springs, while force balance is maintained at the internal nodes.

The geometric structure of a Voronoi network allows for the following set of spring tensions t_i (with i being a spring index) to be a state of self stress:

$$t_i = \eta |C_i^2 - C_i^1|. \quad (\text{E1})$$

Here, η is some constant factor, the vectors C_i^1 and C_i^2 refer to the two Voronoi seed points that are closest to

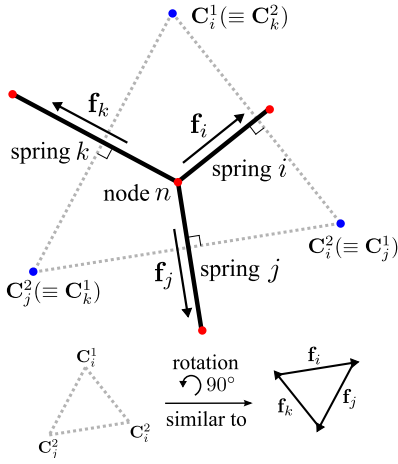


FIG. 7. Illustration of local force balance at a node n of Voronoi networks at creation. Red dots are the internal nodes, while blue dots are the neighboring random seeds used for the Voronoi tessellation. Geometrically, node n is created as the circumcenter of the local triangle (gray dashed lines) formed by these seeds, and the three local springs i , j and k (black segments) are the vertical bisectors of the respective sides. The vectors \mathbf{C}_i^1 and \mathbf{C}_i^2 refer to the two seed points at the side perpendicular to spring i (and similarly for springs j and k). The node n is force-balanced when the magnitude of the spring tensile forces (\mathbf{f}_i , \mathbf{f}_j and \mathbf{f}_k , in black arrows) follow the proportionality relation, Eq. (E1). These forces will form a closed triangle that is similar to the local triangle by a rotation of 90° , thus giving zero net force, see also Eqs. (E2) and (E3).

spring i (Figure 7; i.e. \mathbf{C}_i^1 and \mathbf{C}_i^2 are the two points that generated the line that defines spring i), and $|\cdot|$ denotes the length of a vector.

To show that the set of spring tensions t_i form a state of self stress, we demonstrate that they satisfy local force balance at each node. To this end, we focus here on a node n that is connected to springs i, j, k as shown in Figure 7. The force that spring i exerts on the node n is $\mathbf{f}_i = t_i \mathbf{e}_i$, where \mathbf{e}_i is the unit tangent vector of spring i pointing away from node n . Furthermore, we have

$$\begin{aligned} \mathbf{f}_i &= t_i \mathbf{e}_i \\ &= \eta |\mathbf{C}_i^2 - \mathbf{C}_i^1| \mathbf{e}_i \\ &= \eta |\mathbf{C}_i^2 - \mathbf{C}_i^1| \frac{\mathbf{R}(\pi/2) \cdot (\mathbf{C}_i^2 - \mathbf{C}_i^1)}{|\mathbf{C}_i^2 - \mathbf{C}_i^1|} \quad (\text{E2}) \\ &= \eta \mathbf{R}(\pi/2) \cdot (\mathbf{C}_i^2 - \mathbf{C}_i^1). \end{aligned}$$

Here, in the second line, we inserted the spring tensions Eq. (E1). In the third line, we used the fact that spring i is perpendicular to the segment connected by the two seed points \mathbf{C}_i^1 and \mathbf{C}_i^2 , while the operator $\mathbf{R}(\pi/2)$ performs a counter-clockwise rotation by an angle of $\pi/2$. An analogous equation to Eq. (E2) holds also for the forces by springs j and k . As a consequence, the sum of these three forces is zero:

$$\mathbf{f}_i + \mathbf{f}_j + \mathbf{f}_k = 0. \quad (\text{E3})$$

In other words, force balance on node n holds. This proof is also illustrated at the bottom of Figure 7; up to the factor of proportionality η , the three forces $\mathbf{f}_i, \mathbf{f}_j, \mathbf{f}_k$ correspond to the three triangle sides rotated by $\pi/2$, which is why they add up to zero. Hence, Voronoi networks at creation have a state of self stress given by Eq. (E1).

Appendix F: Apparent non-linear scaling of $\bar{\ell}_{\min}$ in some Delaunay networks

For Delaunay networks with harmonic spring potentials, we observed that a fraction of the networks did not seem to follow the linear relation (D2) between σ_ℓ and $(\bar{\ell} - \ell_0)$ (blue and red data points in Figure 8a inset). This is also apparent from the absence of a plateau in $\sigma_\ell/(\bar{\ell} - \ell_0)$ (compare blue and red with black data points in Figure 8a). From our arguments in appendix D, it follows that this non-linearity also implies a non-linear scaling of the minimal-length function $\bar{\ell}_{\min}$ with σ_ℓ , which would also affect the elastic network properties, Eqs. (18)-(21).

We wondered whether this non-linear scaling between σ_ℓ and $(\bar{\ell} - \ell_0)$ was just due to finite numerical cutoffs, or whether it reflects the real scaling behavior infinitesimally close to the transition point. Numerical limitations arise because we cannot probe the networks arbitrarily close to the true transition point. Indeed, we used a cutoff value of $T_{\text{cutoff}} = 10^{-10}$ for the isotropic stress T to numerically identify the transition point. In other words, at the detected transition point we are already in the rigid regime by some small extent beyond the true transition point. If the plateau in $\sigma_\ell/(\bar{\ell} - \ell_0)$ exists only close to the true transition point until some isotropic stress value $T_{\text{max}} < T_{\text{cutoff}}$, we will not detect it since we missed that regime. To test if this could be the case, we created histograms of the extent T_{max} of the plateau for different connectivity z (Figure 8b). For a given network, we define T_{max} as the isotropic stress of the data point at which the quotient $\sigma_\ell/(\bar{\ell} - \ell_0)$ first deviates by more than 10% from the value of this quotient at the detected transition point. For networks where the plateau ends below T_{cutoff} , we would find with this approach $T_{\text{max}} \approx T_{\text{cutoff}} = 10^{-10}$. If there is a significant excess of networks where we numerically do not observe a plateau, this could be an indication that there is indeed no plateau.

Figure 8b shows that for Delaunay networks with harmonic springs, T_{max} generally decreases with connectivity z , and that we only observe a peak around $T_{\text{max}} \approx T_{\text{cutoff}}$ occur mostly for the two largest values of z . Even in these cases, the peak is not very pronounced and may very well arise from the integral of the real T_{max} distribution from 0 to T_{cutoff} . In other words, these networks may possibly have a plateau which ends just too close to the transition point for us to detect it.

This is also consistent with the observation that most of these curves appear to collapse with the curves that do

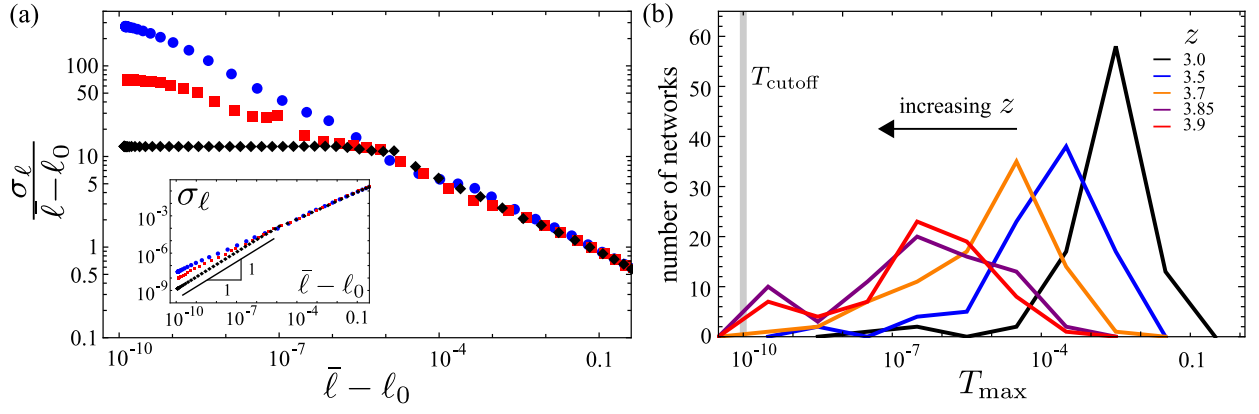


FIG. 8. (a) The quotient $\sigma_\ell/(\bar{\ell} - \ell_0)$ plotted versus $\bar{\ell} - \ell_0$ for Delaunay networks with harmonic spring potentials, shown here for three networks. These networks show either a linear (black diamonds) or non-linear (blue dots and red squares) scaling between σ_ℓ and $\bar{\ell} - \ell_0$ close to the transition point (inset), where a linear scaling is reflected by a plateau in the quotient $\sigma_\ell/(\bar{\ell} - \ell_0)$. (b) Histograms of the extent T_{\max} of the plateau in the quotient $\sigma_\ell/(\bar{\ell} - \ell_0)$ for Delaunay networks with harmonic spring potentials of different connectivity z . We compute T_{\max} as the isotropic stress value where the quotient $\sigma_\ell/(\bar{\ell} - \ell_0)$ starts to show a deviation of more than 10 % from the one computed at the detected transition point. We apply this definition to all networks regardless of the apparent existence of a linear scaling between σ_ℓ and $(\bar{\ell} - \ell_0)$.

show a plateau beyond the end of the plateau (Figure 8a). This suggests that the non-linear scaling regime just cor-

responds to a regime governed by higher order terms. In future work, it will be interesting to see if these higher-order terms could also be predicted from first principles.

-
- [1] W. G. Ellenbroek, Z. Zeravcic, W. Van Saarloos, and M. Van Hecke, *Epl* **87**, 0 (2009), [arXiv:0907.0012](#).
- [2] J. L. Silverberg, A. R. Barrett, M. Das, P. B. Petersen, L. J. Bonassar, and I. Cohen, *Biophysical Journal* **107**, 1721 (2014).
- [3] A. J. Licup, S. Münster, A. Sharma, M. Sheinman, L. M. Jawerth, B. Fabry, D. A. Weitz, and F. C. MacKintosh, *Proceedings of the National Academy of Sciences of the United States of America* **112**, 9573 (2015).
- [4] J. Feng, H. Levine, X. Mao, and L. M. Sander, *Soft Matter* **12**, 1419 (2016).
- [5] A. S. V. Oosten, M. Vahabi, A. J. Licup, A. Sharma, P. A. Galie, F. C. MacKintosh, and P. A. Janmey, *Scientific Reports* **6** (2016), [10.1038/srep19270](#).
- [6] A. Sharma, A. J. Licup, R. Rens, M. Vahabi, K. A. Jansen, G. H. Koenderink, and F. C. MacKintosh, *Physical Review E* **94** (2016), [10.1103/PhysRevE.94.042407](#).
- [7] A. Sharma, A. J. Licup, K. A. Jansen, R. Rens, M. Sheinman, G. H. Koenderink, and F. C. Mackintosh, *Nature Physics* **12**, 584 (2016).
- [8] A. J. Licup, A. Sharma, and F. C. Mackintosh, *Physical Review E* **93** (2016), [10.1103/PhysRevE.93.012407](#).
- [9] K. A. Jansen, A. J. Licup, A. Sharma, R. Rens, F. C. MacKintosh, and G. H. Koenderink, *Biophysical Journal* **114**, 2665 (2018).
- [10] J. L. Shivers, S. Arzash, A. Sharma, and F. C. MacKintosh, *Physical Review Letters* **122** (2019), [10.1103/PhysRevLett.122.188003](#).
- [11] S. Arzash, J. L. Shivers, and F. C. MacKintosh, *Soft Matter* **169**, 6784 (2020).
- [12] J. C. Maxwell, *The London, Edinburgh, and Dublin Philosophical Magazine and Journal of Science* **27**, 294 (1864).
- [13] C. Calladine, *International Journal of Solids and Structures* **14**, 161 (1978).
- [14] T. C. Lubensky, C. L. Kane, X. Mao, A. Souslov, and K. Sun, *Reports Prog. Phys.* **78**, 73901 (2015), [1503.01324](#).
- [15] P. R. Onck, T. Koeman, T. van Dillen, and E. van der Giessen, *Phys. Rev. Lett.* **95**, 178102 (2005).
- [16] M. Wyart, H. Liang, A. Kabla, and L. Mahadevan, *Phys. Rev. Lett.* **101**, 1 (2008), [arXiv:0806.4571v1](#).
- [17] M. Sheinman, C. P. Broedersz, and F. C. MacKintosh, *Physical Review E - Statistical, Nonlinear, and Soft Matter Physics* **85** (2012), [10.1103/PhysRevE.85.021801](#).
- [18] M. F. J. Vermeulen, A. Bose, C. Storm, and W. G. Ellenbroek, *Phys. Rev. E* **96**, 053003 (2017).
- [19] S. Arzash, J. L. Shivers, A. J. Licup, A. Sharma, and F. C. MacKintosh, *Phys. Rev. E* **99**, 042412 (2019).
- [20] M. Merkel, K. Baumgarten, B. P. Tighe, and M. L. Manning, *Proc. Natl. Acad. Sci.* **116**, 6560 (2019).
- [21] S. Alexander, *Physics Reports* **296**, 65 (1998).
- [22] D. E. Ingber, N. Wang, and D. Stamenović, *Reports on Progress in Physics* **77**, 046603 (2014).
- [23] O. K. Damavandi, V. F. Hagh, C. D. Santangelo, and M. L. Manning, *arXiv* (2021), [2102.11310](#).
- [24] M. Merkel and M. L. Manning, *New J. Phys.* **20**, 022002 (2018).
- [25] This is because Eq. (10) can be transformed into:

$$\sigma_L^2 = \frac{1}{16}(2u^2 + 9w^2), \quad (1)$$

where $u = \tilde{x}_1 + \tilde{x}_2$ and $w = \tilde{x}_1 - \tilde{x}_2$. This is the equation of an ellipse whose main axes are diagonally oriented and

scale with σ_L .

- [26] That \bar{L} can become arbitrarily large for given $\sigma_L < L_x/4$ can be shown explicitly by considering a subset of configurations parameterized by two scalars w and h as $\mathbf{r}_1 = (-w/2, h)$ and $\mathbf{r}_2 = (w/2, h)$. Then one can show that the choice

$$w(\sigma_L, h) = -\frac{1}{3}(L_x + 8\sigma_L) + \frac{2}{3}\sqrt{(L_x + 2\sigma_L)^2 + 3h^2}$$

leads to the correct value for the standard deviation of the spring lengths σ_L . Moreover, one can show that for this choice, the relation

$$\bar{L}(\sigma_L, h) = \sigma_L + w(\sigma_L, h)$$

holds, and that $\bar{L}(\sigma_L, h = 0) = \bar{L}_{\min}(\sigma_L)$ with \bar{L}_{\min} given by Eq. (11). Finally, for fixed σ_L , the function $\bar{L}(\sigma_L, h)$ increases monotonically with h without upper bound.

- [27] C. P. Broedersz and F. C. MacKintosh, *Soft Matter* **7**, 3186 (2011), [arXiv:1009.3848](https://arxiv.org/abs/1009.3848).
- [28] S. Dagois-Bohy, B. P. Tighe, J. Simon, S. Henkes, and M. Van Hecke, *Phys. Rev. Lett.* **109**, 1 (2012), [arXiv:1203.3364](https://arxiv.org/abs/1203.3364).
- [29] O. K. Damavandi, M. L. Manning, and J. M. Schwarz, *arXiv* (2021), [arXiv:2110.04343](https://arxiv.org/abs/2110.04343).
- [30] S. B. Lindström, D. A. Vader, A. Kulachenko, and D. A. Weitz, *Phys. Rev. E* **82**, 051905 (2010).
- [31] K. Huang and M. Born, *Proc. R. Soc. Lond., A Math. phys. sci. A* **203**, 178 (1950).
- [32] M. Born and K. Huang, *Am. J. Phys.* **23**, 474 (1955), <https://doi.org/10.1119/1.1934059>.
- [33] A. Lemaître and C. Maloney, *Journal of Statistical Physics* **123**, 415 (2006).